

Decoding the Single-peaked H I Spectra of Low Redshift Post-starburst Galaxies

QIFENG HUANG (黄齐丰),¹ JING WANG (王菁),¹ SARA L. ELLISON,² ZEZHONG LIANG (梁泽众),¹ XUCHEN LIN (林旭辰),¹ AND
DONG YANG (杨冬)¹

¹Kavli Institute for Astronomy and Astrophysics, Peking University, Beijing 100871, China

²Department of Physics & Astronomy, University of Victoria, Finnerty Road, Victoria, BC V8P 1A1, Canada

ABSTRACT

Recent observations with the Five-hundred-meter Aperture Spherical Telescope (FAST) have revealed abundant reservoirs of neutral hydrogen (H I) in low redshift post-starburst galaxies (PSBs), raising the question of why star formation ceases rapidly in these systems. In this study, we present a detailed analysis of the shape of the integrated H I spectra of 67 PSBs. We find that PSBs exhibit significantly higher H I spectral concentration values (K) compared to a matched sample from xGASS, and are more comparable to those of starburst galaxies. By extending our analysis to spatially resolved H I data from THINGS and ATLAS^{3D}, we show that both centrally concentrated H I distributions and dynamically unsettled H I can effectively increase K , while non-axisymmetric structures only contribute to the scatter of the K distribution. Distinguishing between central concentration and dynamically unsettled gas as the origin of high K can be achieved by measuring the spectral asymmetry (A_F), making the K - A_F plane a powerful diagnostic tool for identifying galaxies with unsettled H I using integrated spectra alone. Based on their location in the K - A_F plane, we find that most PSBs are not dominated by unsettled H I, but rather exhibit elevated central gas concentration. Both modes of gas redistribution in PSBs may eventually contribute to their quenching.

Keywords: Galaxies (573), Galaxy evolution (594), Interstellar atomic gas (833), Post-starburst galaxies (2176)

1. INTRODUCTION

Post-starburst galaxies (PSBs) represent a unique galaxy population that have recently experienced a starburst phase, followed by a rapid decline in star formation rates (SFRs). This evolutionary track leaves distinctive features in their optical spectra (Dressler & Gunn 1983; Poggianti et al. 1999; Wild et al. 2007). Due to their unique star formation histories (SFHs) and structural similarities with early-type galaxies (ETGs), low-redshift PSBs are widely regarded as systems caught in the act of quenching—transitioning from the star-forming main sequence to the quiescent state (e.g., Yang et al. 2008; Chen et al. 2022; but see Pawlik et al. 2018, 2019). As such, they serve as critical laboratories for understanding the bimodality of galaxy populations and the physical mechanisms driving galaxy quenching (see French 2021 for a review).

As the fuel for star formation, the interstellar medium (ISM) of PSBs holds key clues to the rapid cessation of star formation in these systems. Previous observational studies have consistently revealed that PSBs retain significant molecular gas reservoirs, which display a suppressed efficiency in transitioning into dense gas and forming stars (Rowlands et al. 2015; Alatalo et al. 2016; French et al. 2018b), with simulations showing similar trends (Davis et al. 2019). In cases where high-resolution observations are available, the molecular gas shows extremely high turbulent pressure, potentially accounting for the low star formation efficiency (SFE) observed in PSBs (Otter et al. 2022; Smercina et al. 2022). By tracking the time evolution following the starburst, it has also been found that the mass budget of star-forming gas in PSBs declines over time (Rowlands et al. 2015; French et al. 2018a). However, this gas depletion cannot be fully explained by either residual star formation (French et al. 2018a) or gas outflows (Alatalo et al. 2015; Fodor et al. 2025). Instead, transitioning from the molecular phase to warmer phases of the ISM, including the H I, is likely necessary to reconcile the current observations.

Studies of PSBs using HI have historically been limited by small sample sizes, shallow detection limits, or atypical environments (Chang et al. 2001; Buyle et al. 2006; Zwaan et al. 2013). It was only recently that Ellison et al. (2025, hereafter E25) provided a comprehensive demographic study of HI content in low-redshift PSBs. By analyzing a mass-complete sample of 68 PSBs, they found significant HI reservoirs, with HI fractions intermediate between those of star-forming galaxies and galaxies in the green valley. The plentiful HI left in PSBs therefore leaves open the possibility of re-igniting future star formation. However, this possibility depends critically on the state (e.g., its dynamics) and location (e.g., still in the disk or expelled towards the halo) of HI.

In principle, the best assessment of the status of the remaining HI in PSBs is via detailed spatial mapping, but unfortunately, spatially resolved HI maps are expensive to obtain. On the other hand, as large extragalactic surveys continue to expand, our samples of integrated (or barely resolved) HI spectra are expanding rapidly (e.g., FASHI; Zhang et al. 2024). Thus, extracting meaningful information from HI spectra becomes essential to probe HI properties in large samples and possibly at cosmic distances (Wang et al. 2020; Yu et al. 2022b; Peng et al. 2023). In this paper, we focus on the concentration (i.e., “peakedness” or kurtosis) of HI spectra following the definition of Yu et al. (2022b, hereafter Y22) as a potential tracer of HI spatial distribution and kinematics. Using public interferometry data from The HI Nearby Galaxy Survey (THINGS; Walter et al. 2008) and the ATLAS^{3D} project (Cappellari et al. 2011; Serra et al. 2012), we evaluate how the spatial distribution of HI influences the concentration of integrated spectra and use this information to interpret the observed spectral shape of PSBs. Through this analysis, we aim to constrain the HI properties of PSBs and distinguish between possible scenarios for their quenching.

This paper is organized as follows. Section 2 describes the data used in this paper and introduces the measurement of spectral concentration of HI. In Section 3, we compare the spectral concentration of PSBs with other galaxy samples. We examine the drivers of spectral concentration and discuss the implications of HI properties in PSBs in Section 4. Finally, we summarize the paper and provide future perspectives in Section 5.

2. DATA AND ANALYSIS

2.1. A mass-complete sample of PSBs

The PSB sample used in this paper is taken from E25. Briefly, they combine traditional E+A PSBs (Goto 2005) and a broader PSB sample selected with the PCA method (Wild et al. 2007; Wilkinson et al. 2022) from the 7th Data Release of Sloan Digital Sky Survey (SDSS; Abazajian et al.

2009). The sample is further limited to a stellar mass range of $\log M_*/M_\odot > 9.5$ and redshift $0.01 < z < 0.04$, yielding 86 PSBs after excluding sources with significant confusion in HI observations. Clean HI spectra are obtained for 43 PSBs at $z < 0.0364$ using FAST (Nan et al. 2011), which targets a detection limit similar to the extended GALEX Arecibo SDSS Survey (xGASS; Catinella et al. 2010, 2018), which can be used as a control sample. For the remaining PSBs, we utilize archival data, including 17 HI spectra from ALFALFA (Giovanelli et al. 2005), 2 from xGASS, and 5 from HI-MaNGA (Masters et al. 2019; Stark et al. 2021). The final sample consists of 67 PSBs with available integrated HI spectra. More details on the sample selection, FAST observations, and data reduction can be found in E25. We note that removing PSBs with HI confusion (25 out of 111; E25) may bias the sample against systems undergoing strong interactions, which can disturb the HI. However, since galaxies with HI confusion are also removed from the comparison sample (Section 2.2), and PSBs are not preferentially found in close pairs at these separations (Ellison et al. 2022), the resulting sample bias is minimized.

For the PSB sample, we use stellar masses from the MPA-JHU catalogs (Kauffmann et al. 2003). We cross-match the sample with the NASA-Sloan Atlas (Blanton et al. 2011) to obtain measurements of optical concentration (C_r), defined as the ratio between the radii enclosing 90% and 50% of the Petrosian flux, and apparent axis ratio $q \equiv b/a$, both measured in r -band. The inclination angles (i) are estimated using the following equation (Hubble 1926), incorporating a stellar mass-dependent intrinsic disk thickness (q_0) from Sánchez-Janssen et al. (2010):

$$\cos^2 i = \frac{q^2 - q_0^2(M_*)}{1 - q_0^2(M_*)}. \quad (1)$$

This method tends to underestimate the inclination angles for spheroid-dominated systems, as is likely the case for some PSBs in our sample with $C_r > 2.6$ (Strateva et al. 2001). Correcting for this bias would further enhance the significance of our results, as we will see in Section 3.

The same catalogs and methods are used to obtain properties of the comparison sample introduced in the next section.

2.2. The comparison sample

xGASS provides a representative sample of low-redshift ($0.01 < z < 0.05$) galaxies with deep, uniform HI observations (Catinella et al. 2018). It serves as a benchmark for evaluating the unique properties of PSBs, given our matched HI detection limits. To construct a sample for comparison with the PSBs, we select HI-detected galaxies from xGASS that do not have a confusion flag ($\text{HI_FLAG} \leq 2$) and are not contaminated by radio frequency interference (Y22). To uniformly remove the HI non-detections in both PSBs and xGASS galaxies, we adopt the updated detection threshold

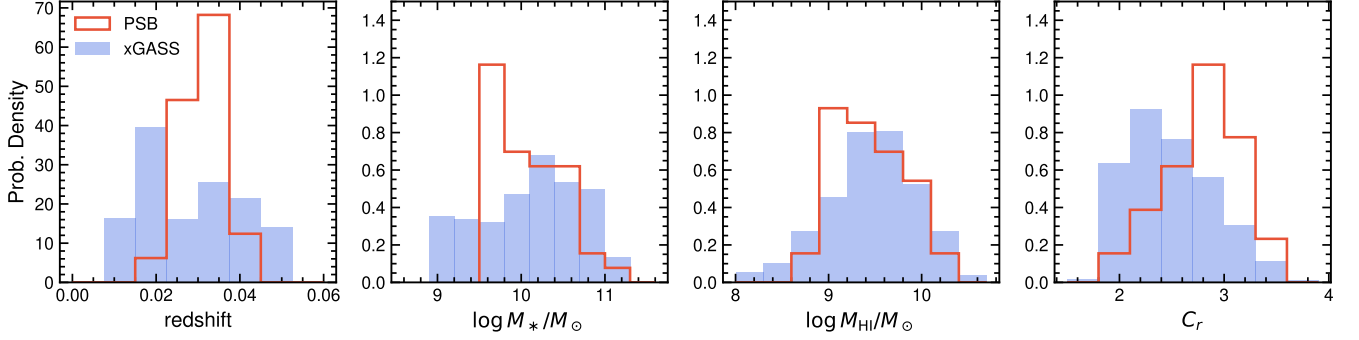


Figure 1. Normalized distributions of sample properties for PSBs (red open) and the comparison sample from xGASS (blue filled).

from E25: $M_{\text{HI}}/M_* > 0.02$ for galaxies with $\log M_*/M_\odot > 10.55$, and $\log M_{\text{HI}}/M_* > 8.85$ at lower stellar masses. This more conservative threshold also excludes marginal HI detections, where the spectral shape cannot be reliably measured. Our final sample includes 43 PSBs and 630 xGASS galaxies that meet these criteria.

Figure 1 presents the normalized distribution of redshift, stellar mass, HI mass, and optical concentration of PSBs and xGASS galaxies. We can see that PSBs occupy a similar parameter space with xGASS, except that they are more likely to have higher optical concentrations. In Section 3, we will control for key galaxy properties for a more robust comparison of the two samples. Our focus is on the concentration of their HI spectra, which is closely related to the spatial distribution of HI, as will be shown later.

2.3. Concentration of integrated HI spectra

The shape of integrated HI spectra can be broadly and qualitatively classified into three categories: double-peaked, flat-topped, and single-peaked. In order to have a more quantitative measure, we use the nonparametric quantity K introduced by Y22 to quantify the concentration of HI spectra. The definition of K is the integrated area between the normalized growth curve—normalized to the point where the flux reaches 85% of the total flux—and the diagonal line of unity (see Figure 2 of Y22). A negative K indicates a double-horned HI spectrum, while a positive value corresponds to a single-peaked spectrum. Flat-topped spectra are characterized by $K \approx 0$. For reference, a Gaussian line profile has $K = 0.079$. A 2-D HI disk with a uniform surface density, a flat rotation curve, and no velocity dispersion has $K = -0.092$. Figure 2 provides some examples of FAST spectra ordered by K . It is clear that the spectra change from double-horned to single-peaked as K increases (from top to bottom panels in Fig. 2). The physical implications of K will be explored in Section 4.

We measure the values of K for all galaxies used in this study and apply the S/N-dependent correction for systematic biases following Y22. The associated uncertainties (σ_K) are

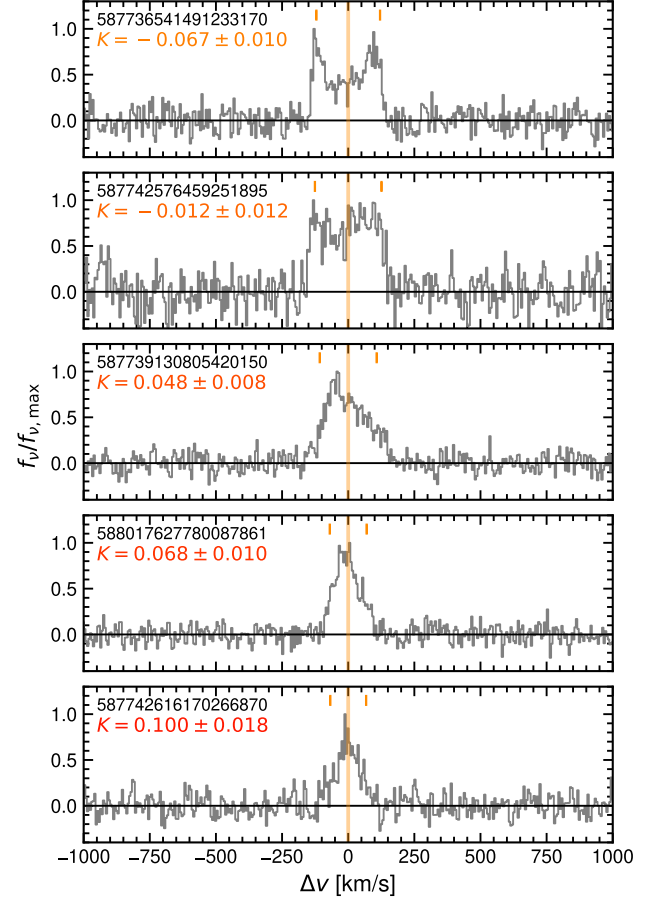


Figure 2. Examples of PSB spectra obtained with FAST, ordered by increasing K and normalized by the peak flux density. Each panel displays the K value and SDSS DR7 objID in the upper left corner. The short orange bars at the top of each panel represent the velocity range of $\Delta v = \pm V_{85}$, where V_{85} is the half width enclosing 85% of the total flux, as defined for K .

estimated by adding random Gaussian noise to the original spectra, which increases the noise level by a factor of $\sim \sqrt{2}$ and makes σ_K a conservative estimate. To minimize systematics between different surveys, we resample the spectra to a

uniform channel width of 5.5 km s^{-1} . For galaxies with ALFALFA spectra, we adopt the K values reported by Y22. To ensure consistency in the measurement procedures, we compare our measurements with those of Y22 for 1000 randomly selected galaxies in their sample, finding negligible systematic offsets (0.001 ± 0.004). The K values of the PSB sample are provided in Appendix D.

3. SINGLE-PEAKED HI SPECTRAL SHAPE OF PSBs

In Figure 3a, we compare the K distributions among the samples defined in Section 2. The offset between PSBs and the xGASS sample clearly shows the peculiarity of PSBs as a special population. While $36.5\% \pm 2.6\%$ galaxies in xGASS exhibit single-peaked HI spectra with $K > 0$, this fraction for the PSBs is almost double ($67.4\% \pm 13.3\%$). Thus, we conclude that most of the low-redshift PSBs in our sample exhibit single-peaked HI spectra.

When relating the spectral concentration K to the spatial distribution of HI, it is important to note that K is influenced by two additional factors besides the HI spatial concentration (e.g., Yu et al. 2022a). First, the relative extent of the rising part of the rotation curve and the HI disk affects the fraction of HI near the central velocity. Second, at lower inclinations, the effect of dispersion-dominated processes (e.g., turbulence and thermal motion) on the spectral shape becomes more significant relative to rotation, leading to a negative correlation between K and the inclination (El-Badry et al. 2018). To ensure a more adequate comparison, we control the related properties (M_* , M_{HI} , C_r , and i ; Yu et al. 2022a) between PSBs and xGASS. As the sample size is limited, a one-to-one matching is not feasible to control four parameters simultaneously. Instead, we subtract the parameter dependence of K by fitting a hyperplane between $\theta = (\log M_*/M_\odot, \log M_{\text{HI}}/M_\odot, C_r, \sin i)$ and K using xGASS:

$$K_0(\theta) = \alpha\theta^T + \beta. \quad (2)$$

Using a Huber regressor that is robust to outliers,¹ we obtain the best-fit parameters $\alpha = (-0.0094, -0.0256, 0.0042, -0.0596)$ and $\beta = 0.352$. The K -excess, denoted as K' , is derived by subtracting K_0 from the original K and provides a fair comparison of HI spectral concentration among different galaxies. By definition, we expect $K' \approx 0$ for a typical galaxy in the xGASS sample. We find no residual dependence of K' on the aforementioned parameters (Appendix A).²

¹ <https://scikit-learn.org/>

² Given the correlation between K and $\sin i$, an uncertainty of 10° in inclination would result in a change of only < 0.01 in K' . Therefore, underestimating the inclination angles of PSBs (Section 2.1) does not affect our results, as the median K' would change by no more than 0.015. This upper limit is obtained by considering the extreme case where all PSBs are edge-on, i.e., where $i = 90^\circ$.

The distributions of K' are shown in Figure 3b, which confirms that PSBs have a higher spectral concentration than the general galaxy population in xGASS. The p -value from a Kolmogorov–Smirnov (K-S) test is smaller than 0.001, indicating a very significant elevation of HI spectral concentration in PSBs. Figure 3b also compares the PSBs with 40 starburst galaxies in xGASS, defined as those lying > 0.4 dex above the star-forming main sequence fitted by Sain-ange et al. (2016). The SFRs are obtained by fitting the far-ultraviolet to mid-infrared broad-band SEDs (Salim et al. 2018). No significant difference is observed between PSBs and starbursts ($p > 0.1$), consistent with previous findings that higher K is usually associated with enhanced star formation activity at a given M_* (Yu et al. 2022a), likely driven by centrally concentrated HI (Wang et al. 2020). This suggests that when galaxies transit from the starburst phase to the PSB phase, the HI distribution and kinematics are retained.

4. DISCUSSION

In the previous section, we demonstrated that PSBs have K (and K') values whose single-peaked nature is more similar to on-going starbursts than “normal” xGASS galaxies. In this section, we investigate the primary drivers of K using spatially resolved HI data (Section 4.1 to 4.4), and discuss the implications of our results on the evolution of PSBs (Section 4.5).

4.1. Spatial concentration of HI

In regularly rotating, dynamically cold HI disks, the spatial concentration of HI is regarded as a critical driver of spectral concentration (Yu et al. 2022a). Although this assumption is intuitive, it has not yet been rigorously tested using spatially resolved HI maps from observations. Here we measure the HI concentration of galaxies from the THINGS survey, which offers high spatial resolution and enables a detailed description of spatial HI distributions (Walter et al. 2008). We use elliptical apertures in the moment-0 maps to calculate the ratio of HI masses within an inner radius (R_{in}) and an outer radius that is twice the size of the inner one ($R_{\text{out}} = 2R_{\text{in}}$). We then measure the K values from the integrated spectra of each galaxy and correct for the inclination angle dependence as in Section 3. Applying inclination measurements from kinematic modeling does not affect our results (e.g., de Blok et al. 2008).

Figure 4a illustrates the relationship between spectral concentration (K') and spatial concentration of HI measured at $R_{\text{in}} = 0.5R_e$, where R_e is the effective radius measured at $3.6 \mu\text{m}$ wavelength (Salo et al. 2015; Sánchez-Alarcón et al. 2025). Nine THINGS galaxies without a measurement of R_e are excluded in the figure. The Pearson- r parameter ($r = 0.69 \pm 0.12$) indicates a strong positive correlation between these quantities, demonstrating that K' effectively

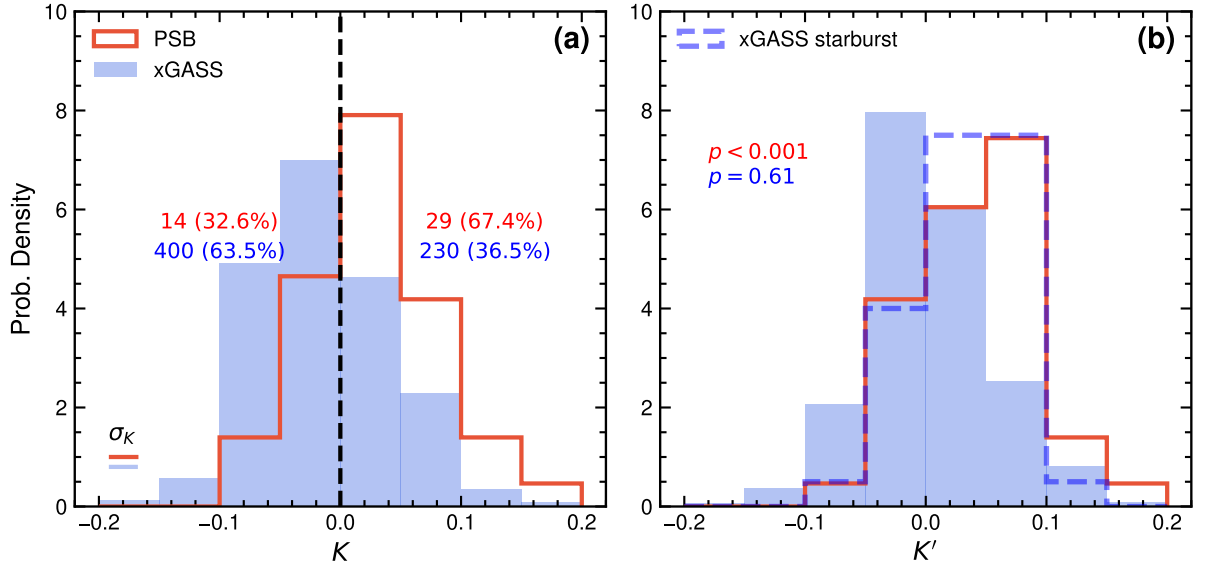


Figure 3. (a) Normalized distribution of K . The same color scheme is used as Figure 1. The short lines in the lower left represent the typical uncertainty in K (σ_K) for each sample. The vertical dashed line marks $K = 0$, the division of single-peaked and double-horned HI spectral shapes. The numbers (percentages) of galaxies in both categories are also provided. (b) Normalized distribution for K' for PSBs, xGASS, and starburst galaxies in xGASS. The p -value in red is evaluated between PSBs and xGASS, while the blue one is calculated between PSBs and the starburst galaxies.

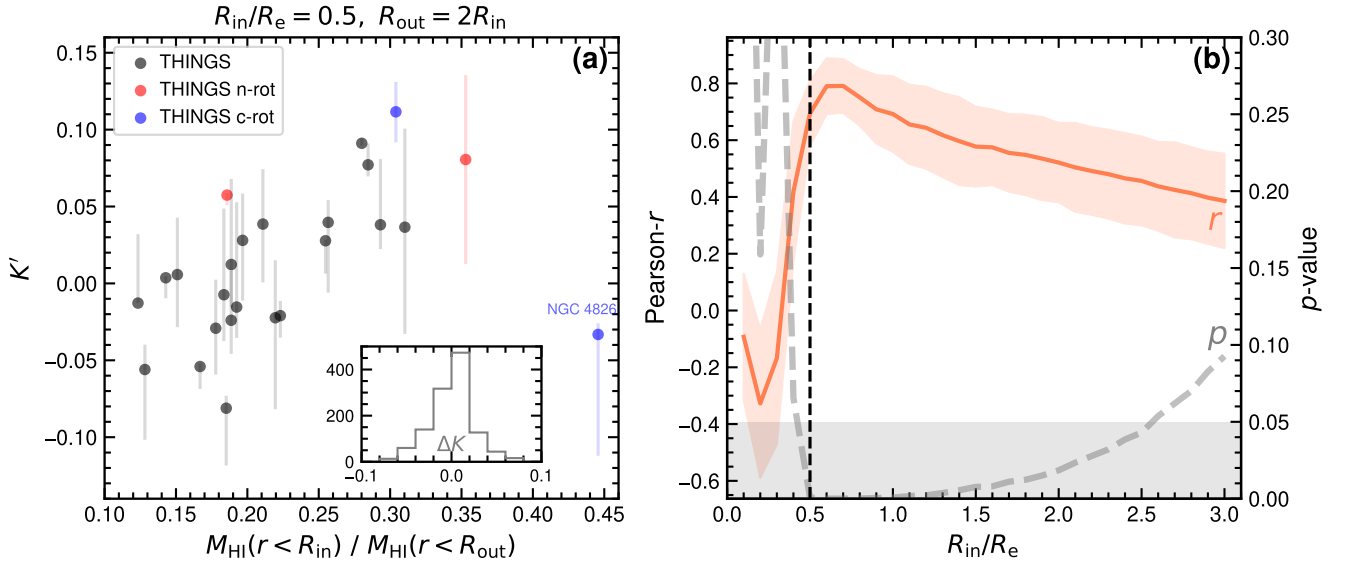


Figure 4. (a) Correlation between K' and the spatial HI concentration for 25 THINGS galaxies. The red and blue dots represent galaxies with no obvious rotation pattern (n-rot) and with counter-rotating HI disks (c-rot), respectively. The error bars and the inset panel display the change in K when artificially rotating the HI mass distribution within the disk plane (see Section 4.2 and Appendix B for details). (b) The Pearson- r correlation coefficients and p -values as a function of R_{in} . The vertical dashed line indicates the radius where panel (a) is plotted. The shaded region at the bottom corresponds to $p < 0.05$. The uncertainties in r are obtained from 1000 bootstraps. The correlation is strongest at $R_{\text{in}} \sim 0.7R_{\text{e}}$ and becomes insignificant at $R_{\text{in}} \gtrsim 2.5R_{\text{e}}$.

traces the spatial concentration of HI in THINGS galaxies.³ To further investigate the radial range to which K' is the most sensitive, we plot the Pearson- r coefficient and the p -value as a function of R_{in} in Figure 4b. We find that the strongest correlation occurs at $R_{\text{in}} \sim 0.7R_e$, while the correlation becomes insignificant at $R_{\text{in}} \gtrsim 2.5R_e$. This result suggests that K' is mainly affected by the HI concentration in the inner disk at $R_{\text{in}} < R_e$, consistent with the fast-rising rotation curves for typical THINGS galaxies (de Blok et al. 2008).

4.2. Non-axisymmetric structures

When observing a rotating galactic disk, regions near the systematic velocity are not limited to the galaxy center but can also appear along the kinematic minor axis and in areas with low radial velocity, often produced by non-axisymmetric structures such as spiral arms and bars. As a result, the spectral concentration K is expected to be altered by the azimuthal inhomogeneity in the HI distribution within the galactic disk.

To mimic random azimuthal variations in HI surface density, we generate mock HI spectra by rotating the THINGS HI moment-0 maps within the disk mid-plane while keeping the moment-1 and moment-2 maps unchanged (see Appendix B for details). We then measure the K values for these mock spectra and calculate the offsets from the original K , denoted as ΔK . In such cases, the amplitudes of the azimuthal variations are inherited directly from realistic galaxies and are representative of galaxies with diverse late-type morphologies, as designed by THINGS (Walter et al. 2008). In Figure 4a, the maximum ranges of ΔK for individual THINGS galaxies are indicated as error bars, and the distribution of ΔK is displayed in the inset panel. The mean and standard deviation of ΔK are -3.5×10^{-5} and 0.024, respectively. These values indicate that while azimuthal variations in HI do not systematically shift the average K for galaxy samples, they contribute to the scatter in K distributions (which is 0.055 for xGASS and 0.053 for PSBs), consistent with the random orientations of real galaxies.

To further evaluate the contribution of different non-axisymmetric components, we manually vary the amplitudes of different Fourier modes within a range of -0.5 to 0.5 dex for each THINGS galaxy (see Appendix B for details) and see how K changes accordingly. Figure 5 illustrates the dependence of ΔK on the amplitude variations in the six leading Fourier modes. The results show that K is mostly affected by the $m = 2$ (dipole) and $m = 1$ (lopsidedness) modes. This behavior is expected because K can be boosted (decreased)

by piling up HI along the kinematic minor (major) axis while removing it in the orthogonal direction. Fourier modes with $m \geq 5$ exhibit negligible effects on K . Moreover, the median ΔK (black dots in Figure 5) for all Fourier modes is consistent with zero, reaffirming that non-axisymmetric structures mainly contribute to the scatter of K rather than systematically altering its value. These results tell us that we can hardly infer the radial distribution of HI for any individual galaxies from K , unless the azimuthal variations are properly accounted for.

4.3. Unsettled HI distribution

In previous sections, we assumed that HI in galaxies is located in a rotating disk, which is not always the case. To extend the THINGS-based analysis to ETGs and consider a broader range of HI morphologies and kinematics, we include the ATLAS^{3D} sample and measure the concentration K of their integrated HI spectra (see Appendix B for details). Besides, we also utilize the spectral asymmetry for all the samples (A_F ; e.g., Bok et al. 2019; Deg et al. 2020; Y22) in the following analysis. A_F is defined as the ratio between the HI flux on one side of the spectral center and the other, requiring $A_F \geq 1$.

In Figure 6a, we plot all the 53 ATLAS^{3D} galaxies with HI detections in the K - A_F plane,⁴ using the same symbols and HI morphological types as in Serra et al. (2012). Galaxies from THINGS (dark red) and xGASS (gray) are also overlaid, along with contours enclosing 50% and 90% of the xGASS galaxies. ETGs with large, regularly rotating HI disk (D -type) occupy a similar locus as xGASS and THINGS galaxies, consistent with their similarities in HI distribution and kinematics. When HI in ETGs is confined to a disk smaller than the stellar disk (d -type) or floating clouds (c -type), its distribution shows a much larger scatter in the plane.

The most striking feature in Figure 6a is that ETGs with unsettled HI morphology and kinematics (u -type; where most HI does not rotate regularly around the stellar body; Morganti et al. 2006; Serra et al. 2012; Lucero & Young 2013) are confined within a narrow region around $K \sim 0.08$ and $A_F \gtrsim 1.2$, suggesting a distinct parameter space for identifying unsettled HI with high purity and completeness. We visually inspect the HI moment maps of galaxies other than the c -type ones and find that two of them can be classified as unsettled (THINGS: NGC 3077; D -type: UGC 3960; see Appendix C). Furthermore, one u -type ETGs outside this region at $A_F < 1.1$ is likely a misclassified d -type (NGC 7280;

³ Galaxies with no rotation pattern in the moment-1 maps (n-rot) and with counter-rotating HI disks (c-rot) are not included in the correlation tests. NGC 4826 deviates significantly from this correlation due to its compact counter-rotating inner disk.

⁴ We use K instead of K' for two reasons. First, K is readily available from HI spectra and does not rely on the sample-dependent fitting result in Equation 2 and the different methods of deriving galaxy properties. Second, the difference between K and K' is small enough ($\sigma_{K_0} = 0.02$ for xGASS). We have tested that using K' does not affect our results.

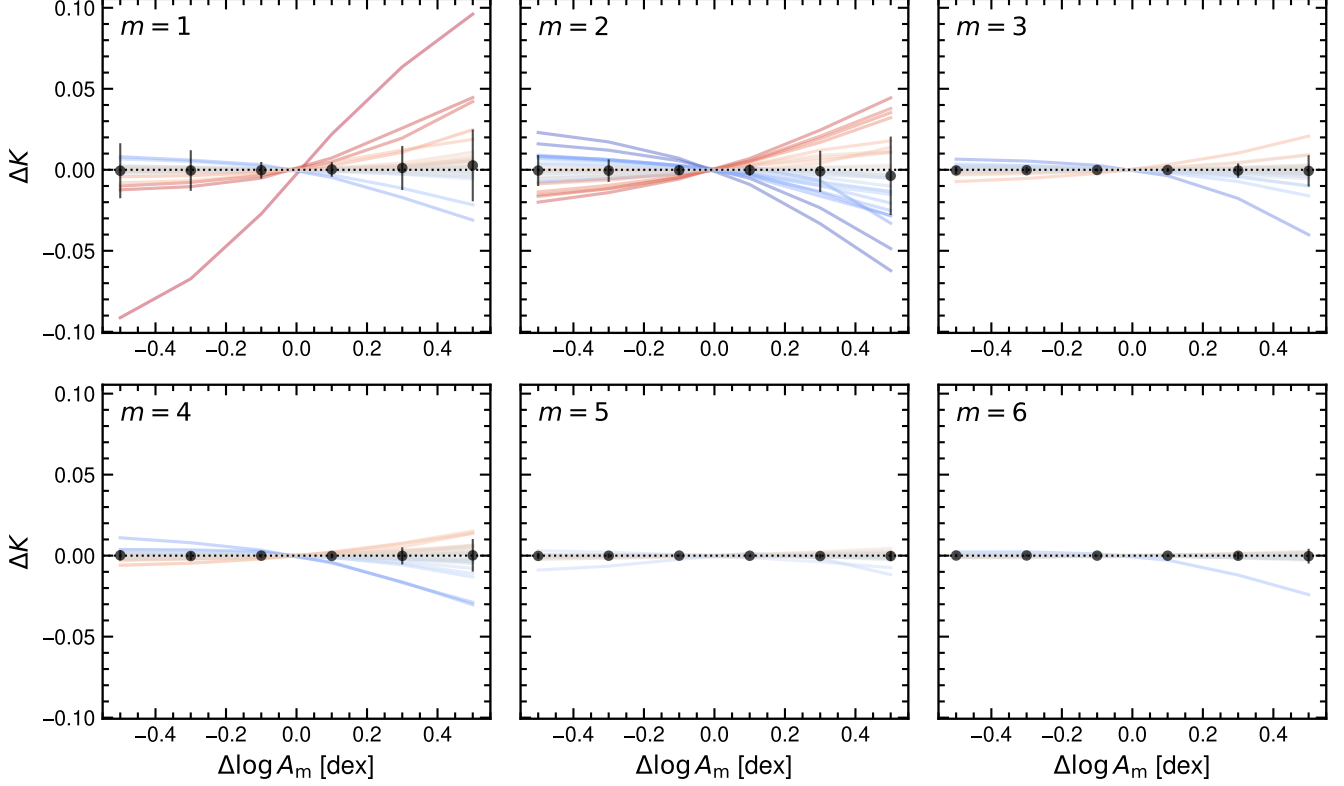


Figure 5. Variations in spectral concentration (ΔK) as a function of changes in Fourier amplitudes ($\Delta \log A_m$) for modes $m = 1$ to $m = 6$. Solid lines represent individual THINGS galaxies, color-coded by the ΔK value at $\Delta \log A_m = 0.5$. Black dots with error bars denote the median values and standard deviations of ΔK for all 34 THINGS galaxies.

Serra et al. 2012). These findings lead us to conclude that external perturbations of HI can increase K by making the HI unsettled, which is usually accompanied by high spectral asymmetry. In Figure 6b, we propose a boundary to separate galaxies with normal (the remaining D -types and THINGS galaxies) and unsettled HI disks using a linear Support Vector Machine, which maximizes the margin between the two classes in the K - A_F plane:

$$A_F > -2.9K + 1.3. \quad (3)$$

We caution, however, that this boundary is empirically derived from THINGS and ATLAS^{3D} galaxies, which are mostly massive and nearby. Care should be taken when applying it to galaxies at higher redshifts or with lower masses. It may also be contaminated by galaxies such as d -type and c -type ones (though these two types of ETGs are more HI-poor; Serra et al. 2012), but is highly confident in excluding D -type galaxies.

4.4. Effects of the missing HI in interferometry data

Interferometry observations like THINGS can filter out the HI with large angular scales and miss those with low column densities (e.g., Pisano 2014; Pingel et al. 2018; Wang et al.

2023). This missing HI component, which accounts for up to $\sim 50\%$ in HI mass for THINGS galaxies, is mostly diffuse and exhibits lagged rotation and higher velocity dispersion (Wang et al. 2024). These properties of diffuse HI lead to an increased fraction of HI around the systematic velocities, thus increasing the value of K .

We use 13 THINGS galaxies observed by the FEASTS project (Wang et al. 2024). Because FEASTS observations have more complete coverage of a few HI disks, we derive K from the following data sets and compare them in Figure 7a: (i) THINGS cubes; (ii) cut-outs of FEASTS cubes within the sky region of THINGS cubes; (iii) FEASTS full cubes with more complete coverage on HI disks for a few galaxies. We use NGC 4449 as an example to demonstrate the differences between these data sets. Comparing (i) and (ii), we find that the inclusion of missing HI slightly increases K by $\Delta K_{+\text{miss}} = 0.013 \pm 0.026$ (Figure 7b; $\Delta K_{+\text{miss}}$ is defined as $K_{(\text{ii})} - K_{(\text{i})}$). This effect can be degenerated with, or partially contribute to the effect of spatial concentrated HI (Section 4.1). On the other hand, a comparison between (ii) and (iii) shows that HI at the very large radii does not affect K significantly. In Figure 7c, we present the relationship between the effect of missing HI on K and the mass fraction

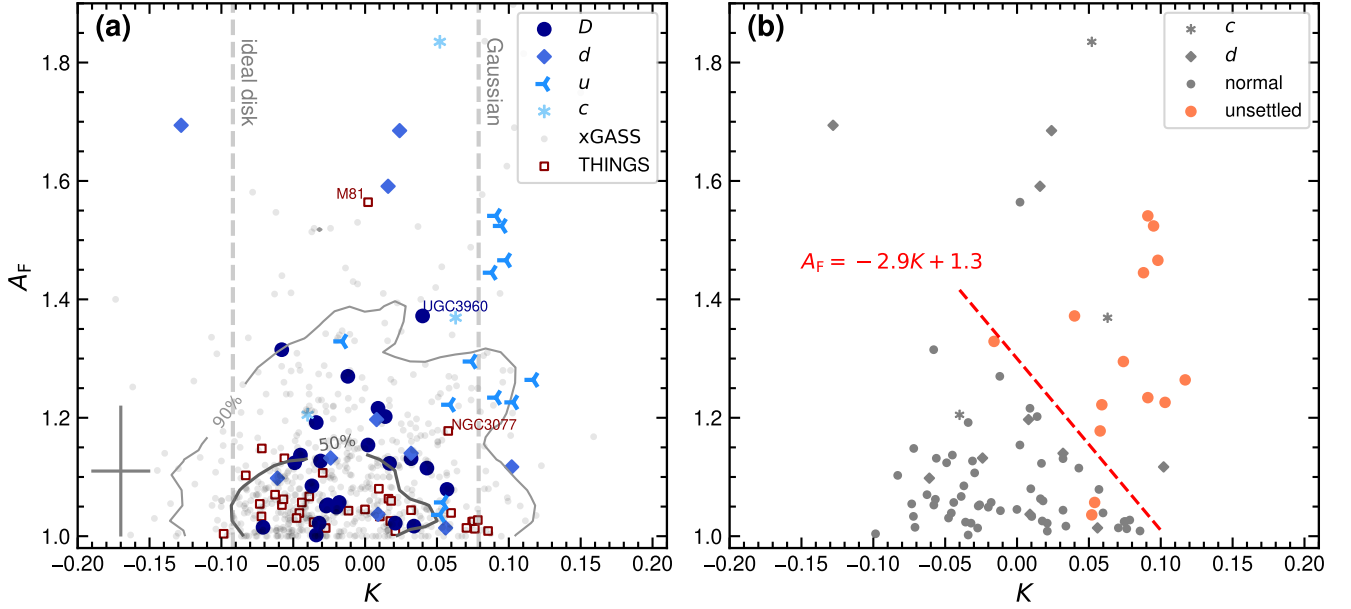


Figure 6. (a) Distribution of galaxies in the K - A_F plane. Galaxies from ATLAS^{3D}, xGASS, and THINGS are shown as blue symbols, gray dots, and dark red squares, respectively. The ATLAS^{3D} symbols follow Serra et al. (2012): D = regularly rotating HI disks larger than the stellar disk, d = regularly rotating HI disks smaller than the stellar disk, u = HI with unsettled morphology/kinematics, and c = HI in small, scattered clouds. The vertical dashed lines mark the K values for an idealized disk and a Gaussian profile (Section 2.3), respectively. Contours enclosing 50% and 90% xGASS galaxies are shown in gray. The typical measurement uncertainty of xGASS is provided in the lower left. (b) ATLAS^{3D} and THINGS galaxies in the K - A_F plane. The unsettled HI disks are highlighted in red, including all the u -types, UGC 3960, and NGC 3077. The remaining galaxies are shown in gray. The red dashed line marks an empirical boundary separating normal (D -types and THINGS) and unsettled HI disks (Equation 3).

of missing HI (f_{miss}). As expected, the value of K changes little for low f_{miss} (< 0.2). At high f_{miss} , however, K exhibits diverse behaviors—it may increase, decrease, or stay relatively constant. This suggests that the specific distribution and kinematics of the missing HI are important in determining K . Future efforts will be needed to enlarge the sample for a better understanding of the conditions driving the diversity.

4.5. How does K reveal the evolution of PSBs?

Based on the previous discussions, we are now in a position to understand how the elevated K values in PSBs are connected to their unique SFHs. As a first attempt, we examine the distribution of PSBs in the K - A_F plane (red symbols in Figure 8a). Less than one-third of the PSBs fall within the region associated with unsettled HI (Equation 3), while the remaining align with the distribution of normal HI disks of xGASS galaxies and D -type ETGs. When we restrict the galaxies to those not classified as unsettled, PSBs still exhibit significantly higher K values compared to xGASS galaxies (Figure 8b; the same holds for K'), with an average K difference of 0.029. For these PSBs, the HI is likely to be more spatially concentrated, supported by a higher level of turbulence, and may be accompanied by a low-density envelope diffusely distributed in the galaxy. Fig. 4 shows that the concentrated HI is likely distributed at $r < R_e$, consistent with

the concentrated CO emission at the central 1 kpc found in low-redshift PSBs (e.g., Otter et al. 2022). CO observations of our PSB sample will be presented in Rasmussen et al. (in prep).

Galaxy mergers are one of the main triggers of low-redshift PSBs (e.g., Sazonova et al. 2021), and they can significantly alter the gas kinematics. Through visual inspection of the optical images from Legacy Surveys (Dey et al. 2019), we identified 18 post-mergers (PMs) from our PSB sample (Appendix D), and the PM fraction ($42\% \pm 10\%$) is consistent with previous studies (e.g., Alatalo et al. 2016; Wilkinson et al. 2022; Ellison et al. 2024). The PMs have a broad distribution in the K - A_F plane (red diamonds in Figure 8a), implying that while violent mergers destroy the HI disks and leave the HI unsettled, mild mergers can also remove angular momentum from the gas and lead to a concentrated gas distribution (e.g., Blumenthal & Barnes 2018; Sparre et al. 2022). Because the HI disk extends further than the stellar disk in gas-rich galaxies, they are more easily disturbed by external forces and tidal features of HI can survive longer than their stellar counterparts. This can explain why, above the threshold defined for unsettled HI, only PSBs located furthest above the line are classified as PMs. Thorp et al. (2024) found that PMs tend to have more concentrated starbursts than their isolated counterparts. It would be interesting to see

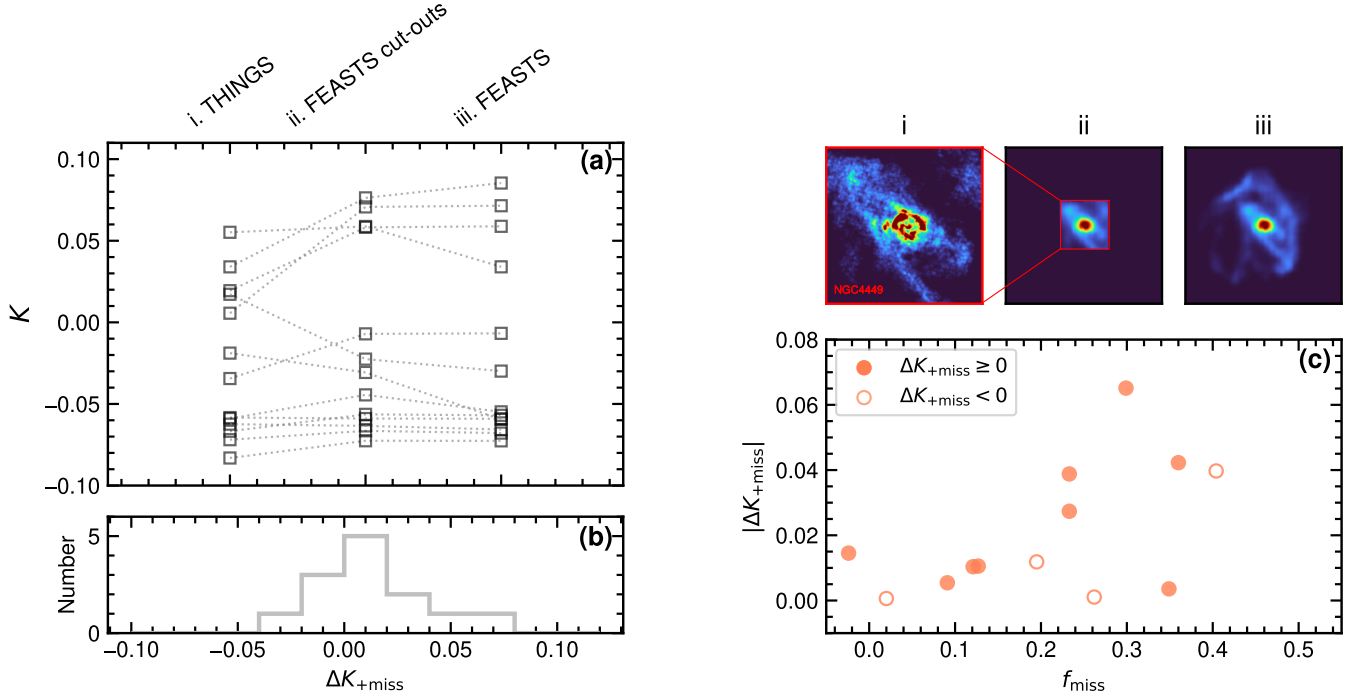


Figure 7. (a) Comparison of K measured with different surveys for 13 galaxies observed with both THINGS and FEASTS. From left to right: (i) THINGS cubes; (ii) cut-outs of FEASTS cubes within the sky region of THINGS cubes; (iii) FEASTS full cubes. An example of the moment-0 maps of the three data sets is shown on the upper right panels. (b) Distribution of differences in K between (i) and (ii) (ΔK_{+miss}). (c) Correlation between $|\Delta K_{+miss}|$ and the mass fraction of missing HI (f_{miss}). The filled dots and open circles represent increased and decreased K after adding HI missed by THINGS, respectively.

if the distribution of HI in PSBs follows the same trend. Unfortunately, this is not possible here due to the limited sample size. Future progress can be made through both increasing the sample size and directly mapping the HI distribution with interferometers.

E25 have demonstrated that PSBs are not devoid of HI. Now we further show that the HI central concentration and gas density are elevated in PSBs, in line with their CO properties. Under such conditions, intense star formation would be expected, which is indeed the case for PSBs in their recent past. From the similarity in the K distributions between PSBs and starburst galaxies (Figure 3b), we can infer that the elevated K and the preceding starburst phase are induced by the same mechanisms such as mergers, and that the HI concentration remains high even after star formation activity has declined. During this process, HI is not significantly ejected from the PSBs by stellar or AGN feedback, as evidenced by the large remaining reservoirs found by E25. Instead, it is stabilized against collapsing and forming stars, likely due to the heating processes (Michałowski et al. 2024), turbulence, or the formation of a spheroidal component during the starburst (Martig et al. 2009). For PSBs with the lowest K , it is possible that the HI will settle into a cold disk and reignite star formation in these galaxies.

5. CONCLUSION

The shape of integrated HI spectra provides valuable information on the distribution and kinematics of neutral gas in galaxies. In this paper, we analyze the spectral concentration (K) of the largest and most complete sample of PSBs with deep HI observations to date, and compare it with the representative xGASS sample. To understand the drivers of spectral concentration, we also construct integrated HI spectra for galaxies with resolved HI maps, including 34 late-type and dwarf galaxies in THINGS and 51 ETGs in ATLAS^{3D}. Several conclusions can be drawn based on our examinations of HI spectral shape:

1. PSBs exhibit significantly higher HI spectral concentrations (K) compared to typical xGASS galaxies, with spectra more likely to be single-peaked rather than double-horned. This conclusion also holds for K' , which removes the dependence of K on other related galaxy properties. The K' distribution of PSBs is comparable to that of starburst galaxies in xGASS.
2. When corrected for inclination angles, K shows a strong correlation with the spatial concentration of HI in THINGS galaxies. This correlation is strongest within the effective radius ($R_{in} \sim 0.7R_e$) and becomes insignificant in the outer disk at $R_{in} \gtrsim 2.5R_e$.

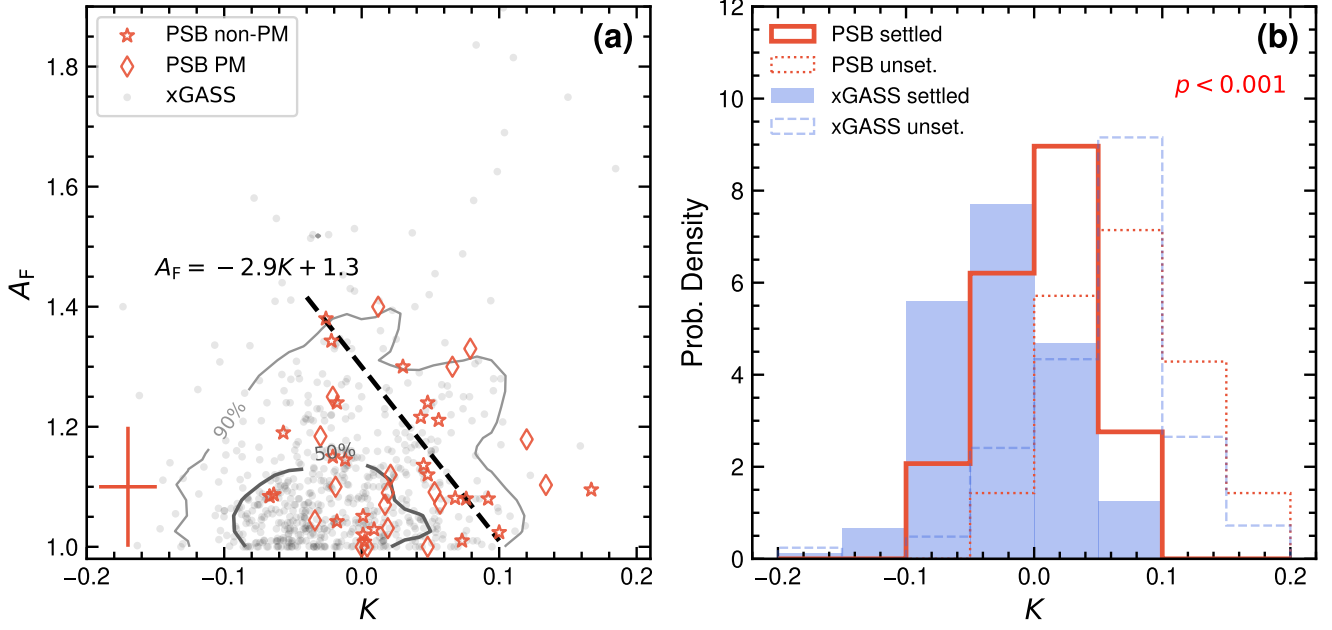


Figure 8. (a) Distributions of PSBs and xGASS galaxies on the K - A_F plane. Contours enclosing 50% and 90% xGASS galaxies are shown in gray, as in Figure 6a. PSBs with and without post-merger (PM) features in their optical images are overlaid using red stars and red diamonds, respectively. The error bar in the lower left represents the typical measurement uncertainty of PSBs. (b) Similar to Figure 3, except that galaxies defined by Equation 3 are separated from their parent samples.

3. Non-axisymmetric structures introduce random variations in K , particularly through the $m = 1$ (lopsidedness) and $m = 2$ (dipole) Fourier modes.
4. Galaxies with unsettled HI distributions display both high K and high spectral asymmetry (A_F). This allows for the identification of such galaxies in the K - A_F plane.
5. Diffuse HI in galaxies can systematically increase K by ~ 0.01 , as it is generally more dispersion dominated than dense HI. For individual galaxies, however, the effect varies depending on the spatial distribution and kinematics of diffuse HI.

Based on these results, we conclude that the elevated K and the quenching of star formation in PSBs likely result from a combination of mechanisms. In around a quarter of the PSBs, star formation ceases mainly because the gas is not in the right position (unsettled). While in the remaining PSBs, the centrally concentrated or diffuse HI suggests that the cold gas is not in the right state to form stars. A significant fraction of post-mergers are identified in both categories, which implies that galaxy interactions play a key role in increasing K by driving gas inflows or disrupting the HI disk. A specific study of how mergers affect the HI spectral shape will be useful, and considering a large sample of spatially resolved HI data is necessary in the future (e.g., WALLABY; Koribalski et al. 2020).

We thank the anonymous referee for valuable comments that improved this manuscript. We thank Vivienne Wild for kindly providing the SDSS spectra fitting results for PSBs. JW thanks support of research grants from Ministry of Science and Technology of the People’s Republic of China (NO. 2022YFA1602902), National Science Foundation of China (NO. 12233001), and the China Manned Space Project (No. CMS-CSST-2025-A08). SLE acknowledges the receipt of an NSERC Discovery Grant.

This work made use of the data from FAST (Five-hundred-meter Aperture Spherical radio Telescope) (<https://cstr.cn/31116.02.FAST>). FAST is a Chinese national mega-science facility, operated by National Astronomical Observatories, Chinese Academy of Sciences. This work is based on data obtained with the Westerbork Synthesis Radio Telescope (WSRT). The WSRT is operated by ASTRON (Netherlands Institute for Radio Astronomy) with support from the Netherlands Foundation for Scientific Research (NWO). The National Radio Astronomy Observatory is a facility of the U.S. National Science Foundation operated under cooperative agreement by Associated Universities, Inc.

The DESI Legacy Imaging Surveys consist of three individual and complementary projects: the Dark Energy Camera Legacy Survey (DECaLS), the Beijing-Arizona Sky Survey (BASS), and the Mayall z-band Legacy Survey (MzLS).

DECaLS, BASS and MzLS together include data obtained, respectively, at the Blanco telescope, Cerro Tololo Inter-American Observatory, NSF's NOIRLab; the Bok telescope, Steward Observatory, University of Arizona; and the Mayall telescope, Kitt Peak National Observatory, NOIRLab. NOIRLab is operated by the Association of Universities for Research in Astronomy (AURA) under a cooperative agreement with the National Science Foundation. Pipeline processing and analyses of the data were supported by NOIRLab and the Lawrence Berkeley National Laboratory (LBNL). Legacy Surveys also uses data products from the Near-Earth Object Wide-field Infrared Survey Explorer (NEOWISE), a project of the Jet Propulsion Laboratory/California In-

stitute of Technology, funded by the National Aeronautics and Space Administration. Legacy Surveys was supported by: the Director, Office of Science, Office of High Energy Physics of the U.S. Department of Energy; the National Energy Research Scientific Computing Center, a DOE Office of Science User Facility; the U.S. National Science Foundation, Division of Astronomical Sciences; the National Astronomical Observatories of China, the Chinese Academy of Sciences and the Chinese National Natural Science Foundation. LBNL is managed by the Regents of the University of California under contract to the U.S. Department of Energy. The complete acknowledgments can be found at <https://www.legacysurvey.org/acknowledgment/>.

APPENDIX

A. DEPENDENCIES OF K

In Section 3, we mentioned that K is dependent on other galaxy properties, and removing these dependencies allows a more adequate comparison between PSBs and xGASS. In the upper panels of Figure 9, we show the correlation between K and M_* , M_{HI} , C_r , and $\sin i$. The lower panels demonstrate that after performing the linear fitting in Equation 2, the K -excess (K') exhibits no significant correlation with these galaxy properties anymore (all $|r| < 0.1$, $p > 0.1$). This suggests that K' is a more robust metric for comparing PSBs to the xGASS sample.

B. DEALING WITH THINGS AND ATLAS^{3D} DATA

Here we describe the detailed procedures for the mock tests discussed in Section 4.2 and the method to obtain the integrated HI spectra for ATLAS^{3D} galaxies (Section 4.3).

B.1. THINGS

The integrated HI spectrum of THINGS are generated by combining the moment-0, moment-1, and moment-2 maps, assuming a Gaussian line profile at each spaxel. For further analysis in Section 4.2, we deproject the observed HI surface density (Σ_{HI}) maps onto the disk plane using the geometry parameters (center, P.A., i) listed in Walter et al. (2008) and assuming that the HI disk is infinitely thin. Then, we perform azimuthal Fourier decomposition on a series of 1-pixel wide annulus to obtain the radial profiles of amplitudes $A_m(r)$ and phase angles $\phi_m(r)$:

$$\Sigma_{\text{HI}}(r, \phi) = \Sigma_0(r) \left\{ 1 + \sum_m A_m(r) \cos[m\phi - \phi_m(r)] \right\}. \quad (\text{B1})$$

To rotate the moment-0 maps in the disk plane, we simply add constant shifts to the phase angles at each radius and reconstruct the deprojected moment-0 maps using Equation B1, which are then projected into the observed frame. The

rotation angle (ϕ_{rot}) ranges from 0° to 350° , with increments of 10° . For each rotated moment-0 map, we generate the corresponding integrated spectrum and measure the spectral concentration K . The ΔK is calculated by subtracting the K value of the $\phi_{\text{rot}} = 0^\circ$ spectrum from that of the target spectrum. Varying the Fourier amplitudes, as in Figure 5, will result in pixels with negative fluxes in the reconstructed maps. In such cases, we set the values of these pixels to zero before generating the integrated HI spectra. The deprojected moment-0 maps are reconstructed using Fourier modes with $m < 20$. The threshold is chosen as a balance between the robustness of the reconstruction and the computational speed.

B.2. ATLAS^{3D}

We use the fully reduced WRST cubes and moment-0 maps⁵ to derive the integrated HI spectra of ATLAS^{3D} galaxies. For each galaxy, its spectrum is extracted from the cube by summing up the spectra at spaxels within the masks of the moment-0 maps. In three galaxies (NGC 680, NGC 3626, NGC 5103), the moment-0 maps of our targets are blended with their neighbors, and we perform a 2-D source de-blending using Photutils (Bradley et al. 2022) to separate the spaxels using the moment-0 maps. A 3-D de-blending method will not improve the results significantly in these cases, as the HI disks are well separated in the projected sky plane (Huang et al. 2025).

C. MOMENT-0 MAPS OF NGC 3077 AND UGC 3960

Figure 10 shows the HI moment-0 maps of two galaxies classified as unsettled: (1) NGC 3077, the D -type ATLAS^{3D} galaxy closest to the locus of u -types in the K - A_F plane; and (2) UGC 3960, the THINGS galaxy closest to the locus of u -types in the K - A_F plane (Figure 6a).

⁵ <https://www-astro.physics.ox.ac.uk/atlas3d/>

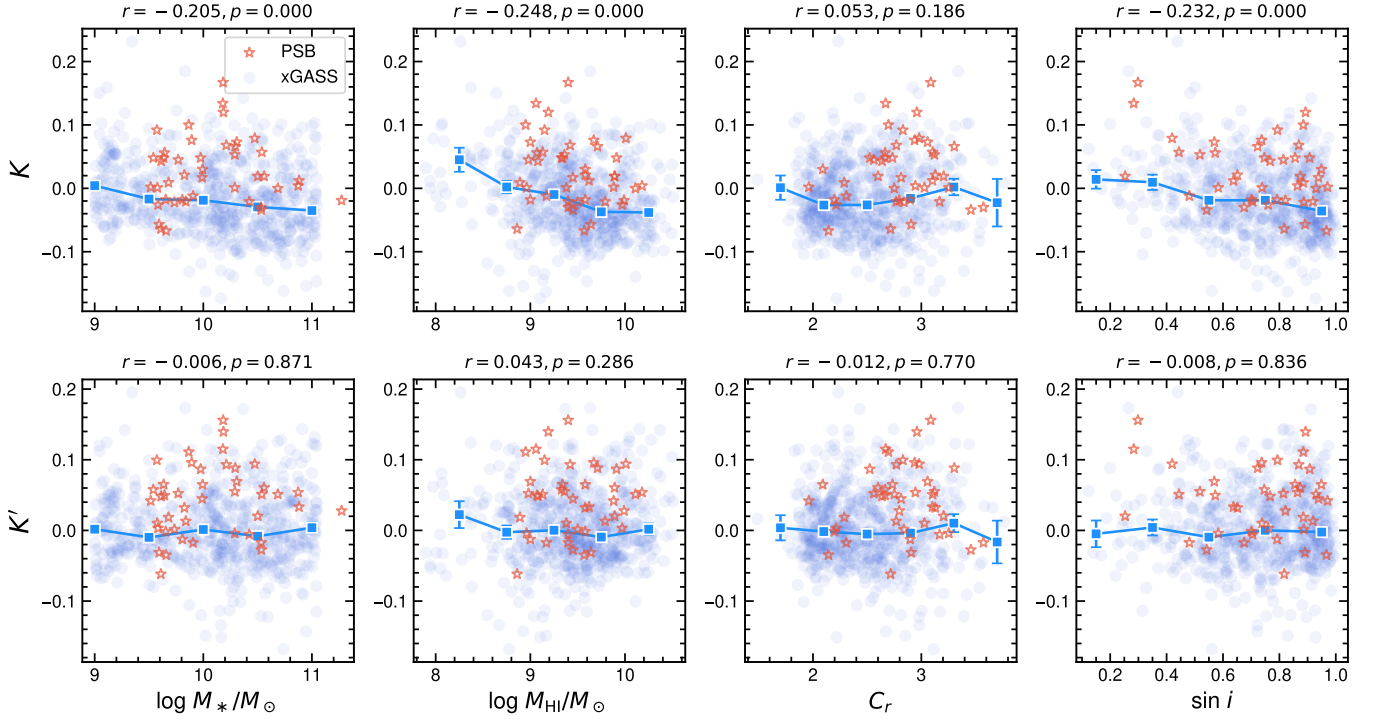


Figure 9. Dependence of K (upper) and K' (lower) on stellar mass, HI mass, optical concentration, and inclination angle. Blue dots and red stars represent xGASS galaxies and PSBs, respectively. The Pearson- r coefficient and the p -value for xGASS are shown at the top of each panel. The median trends of xGASS are plotted as solid blue lines.

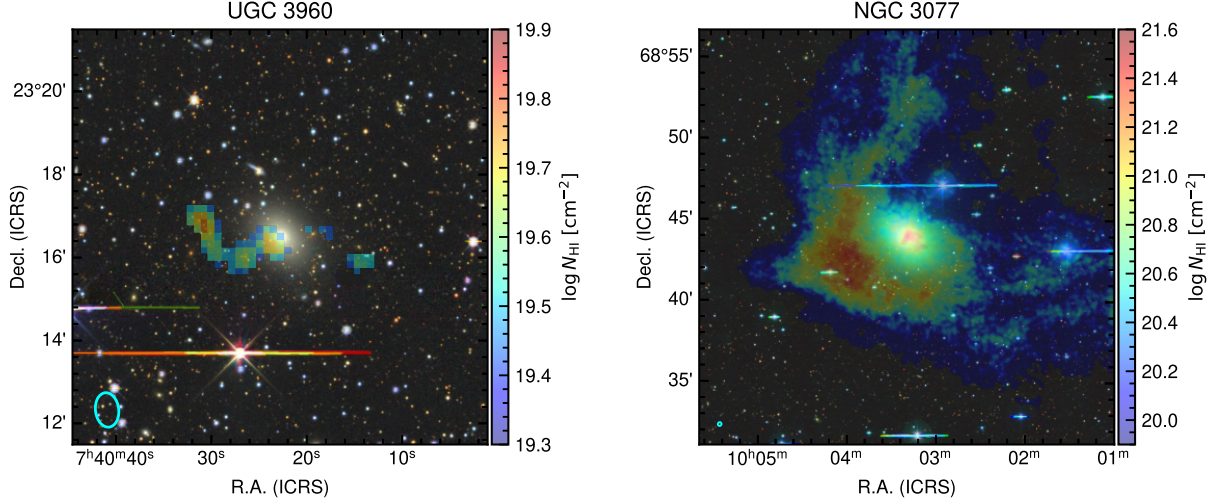


Figure 10. The HI moment-0 maps of UGC 3960 (left; ATLAS^{3D}) and NGC 3077 (right; THINGS). The background images are from the Legacy Surveys (Dey et al. 2019). The cyan circles in the lower left indicate the synthesized beam.

D. PROPERTIES OF THE PSB SAMPLE

Table 1 presents the K values and morphology flags for the PSB sample. The flags are obtained through visually in-

specting the optical images from Legacy Surveys (Dey et al. 2019).

REFERENCES

- Abazajian, K. N., Adelman-McCarthy, J. K., Agüeros, M. A., et al. 2009, *ApJS*, 182, 543, doi: [10.1088/0067-0049/182/2/543](https://doi.org/10.1088/0067-0049/182/2/543)
- Alatalo, K., Lacy, M., Lanz, L., et al. 2015, *ApJ*, 798, 31, doi: [10.1088/0004-637X/798/1/31](https://doi.org/10.1088/0004-637X/798/1/31)

Table 1. Properties of 43 PSBs in the final PSB sample.

SDSS objID	R.A. (deg)	Decl. (deg)	z	$\log M_*$ (M_\odot)	$\log M_{\text{HI}}$ (M_\odot)	PM flag	K	K'	σ_K
(1)	(2)	(3)	(4)	(5)	(6)	(7)	(8)	(9)	(10)
587722984440463382	216.5541	0.8606	0.03186	10.18	9.06	T	0.134	0.115	0.048
587725489988960505	257.1393	57.4767	0.02961	9.61	8.86	F	-0.064	-0.062	0.042
587726032256630848	198.4683	2.1326	0.03026	10.53	9.40	T	-0.030	-0.017	0.028
587729652890206755	256.4333	31.4138	0.03480	9.81	9.00	F	-0.018	-0.013	0.020
587730023333232703	230.5217	5.8549	0.03564	10.50	9.89	T	0.019	0.020	0.018
587730773885059094	351.2256	14.2152	0.02563	9.99	9.45	T	0.017	0.045	0.023
587730847963545655	318.5023	0.5351	0.02692	10.18	9.40	F	0.167	0.156	0.054
587731174382502294	319.9507	0.6727	0.03442	9.61	9.08	F	0.043	0.048	0.057
587731186735186207	347.2619	0.2669	0.03252	10.19	9.19	T	0.120	0.140	0.015
587731886809808959	123.8574	37.3405	0.03975	9.89	9.67	F	0.076	0.096	0.048
587732580982521898	169.7818	58.0540	0.03260	10.54	9.13	T	0.057	0.051	0.023
587734622705811566	131.1576	32.9064	0.03154	10.31	9.00	F	0.073	0.069	0.018
587734891673026666	165.3640	8.4206	0.03061	9.84	9.79	F	-0.021	0.013	0.020
587732771584671859	164.5907	9.4539	0.03359	9.77	8.98	F	0.045	0.052	0.037
587735347486457882	149.9206	11.5331	0.03669	10.42	9.40	T	-0.021	-0.006	0.037
587735664773431424	226.1544	48.7388	0.03610	10.53	9.45	T	-0.034	-0.027	0.009
587736584980463705	251.1281	19.9408	0.02300	10.29	9.36	T	0.053	0.055	0.037
587736541491233170	237.7184	5.3269	0.02603	9.66	9.57	F	-0.067	-0.035	0.010
587736808838594663	207.9975	13.9675	0.03669	11.27	9.99	T	-0.019	0.028	0.021
587738615415373880	170.9459	35.4423	0.03407	10.29	8.96	F	0.001	-0.004	0.017
587739130805420150	206.4464	34.4932	0.03479	9.54	9.33	F	0.048	0.058	0.008
587739504477077652	204.0172	30.1411	0.02593	9.64	9.07	F	0.056	0.050	0.016
587739646208770144	168.9029	30.4228	0.02788	9.65	9.58	F	-0.018	-0.002	0.034
587739828743962776	228.0094	21.2982	0.01578	10.69	10.11	T	-0.000	0.051	0.015
587739845393186912	240.2146	15.1513	0.03396	10.47	10.01	T	0.079	0.094	0.032
587741532777152653	149.7504	25.1031	0.02209	9.57	9.15	F	0.092	0.099	0.043
587741721214386184	197.9218	26.3901	0.03811	9.98	9.91	T	0.048	0.087	0.033
587742010042744920	121.1948	10.7783	0.03526	10.87	10.18	T	0.004	0.054	0.017
587742189908983921	194.5416	24.3489	0.02267	9.58	9.38	F	0.001	0.010	0.021
587742576459251895	225.3402	15.2499	0.03537	9.91	9.17	F	-0.012	-0.017	0.012
587742551762796902	238.8105	12.9163	0.03291	9.58	9.97	F	-0.026	0.003	0.021
587742616170266870	235.7542	16.9874	0.03141	9.87	8.95	F	0.100	0.111	0.018
587742627998531885	246.2755	8.3820	0.03511	10.29	9.71	T	0.066	0.088	0.033
587742628523475193	219.3072	14.6651	0.03790	10.88	9.62	T	0.012	0.033	0.042
587745244159082657	136.4664	13.7175	0.02735	9.68	8.89	F	0.009	0.019	0.037
588015508189872263	346.9322	-0.8385	0.03253	9.52	9.88	F	0.002	0.042	0.003
588016891172618376	147.9371	35.6221	0.02705	10.56	9.89	T	0.019	0.060	0.005
588017627780087861	227.2295	37.5583	0.02906	10.21	9.42	F	0.068	0.093	0.010
588017724947759115	208.8698	6.5964	0.02408	9.83	9.58	T	0.021	0.032	0.019
588848898848784582	202.5796	-0.8707	0.03760	9.73	9.50	F	-0.022	0.001	0.041
588017992299380883	202.2052	10.3817	0.02310	9.59	9.64	F	-0.057	-0.031	0.017
588023046941245549	139.1146	19.9205	0.02598	9.99	9.58	F	0.030	0.065	0.021
588298664112881826	192.6636	47.9343	0.02911	9.63	9.34	F	0.048	0.065	0.027

NOTE—Columns: (1) SDSS DR7 ObjID. (2) Right ascension. (3) Declination. (4) Redshift from SDSS DR7 optical spectrum. (5) Stellar mass from the MPA-JHU catalogs. (6) HI mass from E25. (7) Visual identification of post-mergers. (8) Concentration of the HI spectra. (9) The K -excess, defined as $K - K_0$ (Section 3). (10) Uncertainty of K .

- Alatalo, K., Lisenfeld, U., Lanz, L., et al. 2016, *ApJ*, 827, 106, doi: [10.3847/0004-637X/827/2/106](https://doi.org/10.3847/0004-637X/827/2/106)
- Blanton, M. R., Kazin, E., Muna, D., Weaver, B. A., & Price-Whelan, A. 2011, *AJ*, 142, 31, doi: [10.1088/0004-6256/142/1/31](https://doi.org/10.1088/0004-6256/142/1/31)
- Blumenthal, K. A., & Barnes, J. E. 2018, *MNRAS*, 479, 3952, doi: [10.1093/mnras/sty1605](https://doi.org/10.1093/mnras/sty1605)
- Bok, J., Blyth, S.-L., Gilbank, D. G., & Elson, E. C. 2019, *MNRAS*, 484, 582, doi: [10.1093/mnras/sty3448](https://doi.org/10.1093/mnras/sty3448)
- Bradley, L., Sipőcz, B., Robitaille, T., et al. 2022, *Astropy/Photutils*: 1.5.0, Zenodo, doi: [10.5281/zenodo.6825092](https://doi.org/10.5281/zenodo.6825092)
- Buyle, P., Michielsen, D., De Rijcke, S., et al. 2006, *ApJ*, 649, 163, doi: [10.1086/505633](https://doi.org/10.1086/505633)
- Cappellari, M., Emsellem, E., Krajnović, D., et al. 2011, *MNRAS*, 413, 813, doi: [10.1111/j.1365-2966.2010.18174.x](https://doi.org/10.1111/j.1365-2966.2010.18174.x)
- Catinella, B., Schiminovich, D., Kauffmann, G., et al. 2010, *MNRAS*, 403, 683, doi: [10.1111/j.1365-2966.2009.16180.x](https://doi.org/10.1111/j.1365-2966.2009.16180.x)
- Catinella, B., Saintonge, A., Janowiecki, S., et al. 2018, *MNRAS*, 476, 875, doi: [10.1093/mnras/sty089](https://doi.org/10.1093/mnras/sty089)
- Chang, T.-C., van Gorkom, J. H., Zabludoff, A. I., Zaritsky, D., & Mihos, J. C. 2001, *AJ*, 121, 1965, doi: [10.1086/319959](https://doi.org/10.1086/319959)
- Chen, X., Lin, Z., Kong, X., et al. 2022, *ApJ*, 933, 228, doi: [10.3847/1538-4357/ac75b4](https://doi.org/10.3847/1538-4357/ac75b4)
- Davis, T. A., van de Voort, F., Rowlands, K., et al. 2019, *MNRAS*, 484, 2447, doi: [10.1093/mnras/stz180](https://doi.org/10.1093/mnras/stz180)
- de Blok, W. J. G., Walter, F., Brinks, E., et al. 2008, *The Astronomical Journal*, 136, 2648, doi: [10.1088/0004-6256/136/6/2648](https://doi.org/10.1088/0004-6256/136/6/2648)
- Deg, N., Blyth, S. L., Hank, N., Kruger, S., & Carignan, C. 2020, *MNRAS*, 495, 1984, doi: [10.1093/mnras/staa1368](https://doi.org/10.1093/mnras/staa1368)
- Dey, A., Schlegel, D. J., Lang, D., et al. 2019, *AJ*, 157, 168, doi: [10.3847/1538-3881/ab089d](https://doi.org/10.3847/1538-3881/ab089d)
- Dressler, A., & Gunn, J. E. 1983, *ApJ*, 270, 7, doi: [10.1086/161093](https://doi.org/10.1086/161093)
- El-Badry, K., Bradford, J., Quataert, E., et al. 2018, *MNRAS*, 477, 1536, doi: [10.1093/mnras/sty730](https://doi.org/10.1093/mnras/sty730)
- Ellison, S., Ferreira, L., Wild, V., et al. 2024, *OJAp*, 7, 121, doi: [10.33232/001c.127779](https://doi.org/10.33232/001c.127779)
- Ellison, S. L., Wilkinson, S., Woo, J., et al. 2022, *MNRAS*, 517, L92, doi: [10.1093/mnras/slac109](https://doi.org/10.1093/mnras/slac109)
- Ellison, S. L., Huang, Q., Yang, D., et al. 2025, *Low Redshift Post-Starburst Galaxies Host Abundant HI Reservoirs*, arXiv, doi: [10.48550/arXiv.2503.03066](https://doi.org/10.48550/arXiv.2503.03066)
- Fodor, A., Tomko, T., Braun, M., et al. 2025, *ApJ*, 979, 94, doi: [10.3847/1538-4357/ad900f](https://doi.org/10.3847/1538-4357/ad900f)
- French, K. D. 2021, *PASP*, 133, 072001, doi: [10.1088/1538-3873/ac0a59](https://doi.org/10.1088/1538-3873/ac0a59)
- French, K. D., Yang, Y., Zabludoff, A. I., & Tremonti, C. A. 2018a, *ApJ*, 862, 2, doi: [10.3847/1538-4357/aacb2d](https://doi.org/10.3847/1538-4357/aacb2d)
- French, K. D., Zabludoff, A. I., Yoon, I., et al. 2018b, *ApJ*, 861, 123, doi: [10.3847/1538-4357/aac8de](https://doi.org/10.3847/1538-4357/aac8de)
- Giovanelli, R., Haynes, M. P., Kent, B. R., et al. 2005, *AJ*, 130, 2598, doi: [10.1086/497431](https://doi.org/10.1086/497431)
- Goto, T. 2005, *MNRAS*, 357, 937, doi: [10.1111/j.1365-2966.2005.08701.x](https://doi.org/10.1111/j.1365-2966.2005.08701.x)
- Huang, Q., Wang, J., Lin, X., et al. 2025, *ApJ*, 980, 157, doi: [10.3847/1538-4357/ad9579](https://doi.org/10.3847/1538-4357/ad9579)
- Hubble, E. P. 1926, *ApJ*, 64, 321, doi: [10.1086/143018](https://doi.org/10.1086/143018)
- Kauffmann, G., Heckman, T. M., White, S. D. M., et al. 2003, *MNRAS*, 341, 33, doi: [10.1046/j.1365-8711.2003.06291.x](https://doi.org/10.1046/j.1365-8711.2003.06291.x)
- Koribalski, B. S., Staveley-Smith, L., Westmeier, T., et al. 2020, *Ap&SS*, 365, 118, doi: [10.1007/s10509-020-03831-4](https://doi.org/10.1007/s10509-020-03831-4)
- Lucero, D. M., & Young, L. M. 2013, *AJ*, 145, 56, doi: [10.1088/0004-6256/145/3/56](https://doi.org/10.1088/0004-6256/145/3/56)
- Martig, M., Bournaud, F., Teyssier, R., & Dekel, A. 2009, *ApJ*, 707, 250, doi: [10.1088/0004-637X/707/1/250](https://doi.org/10.1088/0004-637X/707/1/250)
- Masters, K. L., Stark, D. V., Pace, Z. J., et al. 2019, *MNRAS*, 488, 3396, doi: [10.1093/mnras/stz1889](https://doi.org/10.1093/mnras/stz1889)
- Michałowski, M. J., Gall, C., Hjorth, J., et al. 2024, *ApJ*, 964, 129, doi: [10.3847/1538-4357/ad1b52](https://doi.org/10.3847/1538-4357/ad1b52)
- Morganti, R., de Zeeuw, P. T., Oosterloo, T. A., et al. 2006, *MNRAS*, 371, 157, doi: [10.1111/j.1365-2966.2006.10681.x](https://doi.org/10.1111/j.1365-2966.2006.10681.x)
- Nan, R., Li, D., Jin, C., et al. 2011, *Int. J. Mod. Phys. D*, 20, 989, doi: [10.1142/S0218271811019335](https://doi.org/10.1142/S0218271811019335)
- Otter, J. A., Rowlands, K., Alatalo, K., et al. 2022, *ApJ*, 941, 93, doi: [10.3847/1538-4357/ac9dee](https://doi.org/10.3847/1538-4357/ac9dee)
- Pawlik, M. M., McAlpine, S., Trayford, J. W., et al. 2019, *Nat. Astron.*, 3, 440, doi: [10.1038/s41550-019-0725-z](https://doi.org/10.1038/s41550-019-0725-z)
- Pawlik, M. M., Taj Aldeen, L., Wild, V., et al. 2018, *MNRAS*, 477, 1708, doi: [10.1093/mnras/sty589](https://doi.org/10.1093/mnras/sty589)
- Peng, B., Haynes, M. P., Ball, C. J., & Jones, M. G. 2023, *ApJ*, 950, 163, doi: [10.3847/1538-4357/accb51](https://doi.org/10.3847/1538-4357/accb51)
- Pingel, N. M., Pisano, D. J., Heald, G., et al. 2018, *ApJ*, 865, 36, doi: [10.3847/1538-4357/aad816](https://doi.org/10.3847/1538-4357/aad816)
- Pisano, D. J. 2014, *AJ*, 147, 48, doi: [10.1088/0004-6256/147/3/48](https://doi.org/10.1088/0004-6256/147/3/48)
- Poggianti, B. M., Smail, I., Dressler, A., et al. 1999, *ApJ*, 518, 576, doi: [10.1086/307322](https://doi.org/10.1086/307322)
- Rowlands, K., Wild, V., Nesvadba, N., et al. 2015, *MNRAS*, 448, 258, doi: [10.1093/mnras/stu2714](https://doi.org/10.1093/mnras/stu2714)
- Saintonge, A., Catinella, B., Cortese, L., et al. 2016, *MNRAS*, 462, 1749, doi: [10.1093/mnras/stw1715](https://doi.org/10.1093/mnras/stw1715)
- Salim, S., Boquien, M., & Lee, J. C. 2018, *ApJ*, 859, 11, doi: [10.3847/1538-4357/aabf3c](https://doi.org/10.3847/1538-4357/aabf3c)
- Salo, H., Laurikainen, E., Laine, J., et al. 2015, *Astrophys. J. Suppl. Ser.*, 219, 4, doi: [10.1088/0067-0049/219/1/4](https://doi.org/10.1088/0067-0049/219/1/4)
- Sánchez-Alarcón, P. M., Salo, H., Knapen, J. H., et al. 2025, *The Complete Spitzer Survey of Stellar Structure in Galaxies (CS\$^4\$G)*, arXiv, doi: [10.48550/arXiv.2503.09680](https://doi.org/10.48550/arXiv.2503.09680)
- Sánchez-Janssen, R., Méndez-Abreu, J., & Aguerri, J. A. L. 2010, *MNRAS*, 406, L65, doi: [10.1111/j.1745-3933.2010.00883.x](https://doi.org/10.1111/j.1745-3933.2010.00883.x)

- Sazonova, E., Alatalo, K., Rowlands, K., et al. 2021, *ApJ*, 919, 134, doi: [10.3847/1538-4357/ac0f7f](https://doi.org/10.3847/1538-4357/ac0f7f)
- Serra, P., Oosterloo, T., Morganti, R., et al. 2012, *MNRAS*, 422, 1835, doi: [10.1111/j.1365-2966.2012.20219.x](https://doi.org/10.1111/j.1365-2966.2012.20219.x)
- Smercina, A., Smith, J.-D. T., French, K. D., et al. 2022, *ApJ*, 929, 154, doi: [10.3847/1538-4357/ac5d5f](https://doi.org/10.3847/1538-4357/ac5d5f)
- Sparre, M., Whittingham, J., Damle, M., et al. 2022, *MNRAS*, 509, 2720, doi: [10.1093/mnras/stab3171](https://doi.org/10.1093/mnras/stab3171)
- Stark, D. V., Masters, K. L., Avila-Reese, V., et al. 2021, *MNRAS*, 503, 1345, doi: [10.1093/mnras/stab566](https://doi.org/10.1093/mnras/stab566)
- Strateva, I., Ivezić, Ž., Knapp, G. R., et al. 2001, *AJ*, 122, 1861, doi: [10.1086/323301](https://doi.org/10.1086/323301)
- Thorp, M. D., Ellison, S. L., & Galicia, A. 2024, *A&A*, 690, L4, doi: [10.1051/0004-6361/202451662](https://doi.org/10.1051/0004-6361/202451662)
- Walter, F., Brinks, E., de Blok, W. J. G., et al. 2008, *AJ*, 136, 2563, doi: [10.1088/0004-6256/136/6/2563](https://doi.org/10.1088/0004-6256/136/6/2563)
- Wang, J., Catinella, B., Saintonge, A., et al. 2020, *ApJ*, 890, 63, doi: [10.3847/1538-4357/ab68dd](https://doi.org/10.3847/1538-4357/ab68dd)
- Wang, J., Yang, D., Oh, S. H., et al. 2023, *ApJ*, 944, 102, doi: [10.3847/1538-4357/acafe8](https://doi.org/10.3847/1538-4357/acafe8)
- Wang, J., Lin, X., Yang, D., et al. 2024, *ApJ*, 968, 48, doi: [10.3847/1538-4357/ad3e61](https://doi.org/10.3847/1538-4357/ad3e61)
- Wild, V., Kauffmann, G., Heckman, T., et al. 2007, *MNRAS*, 381, 543, doi: [10.1111/j.1365-2966.2007.12256.x](https://doi.org/10.1111/j.1365-2966.2007.12256.x)
- Wilkinson, S., Ellison, S. L., Bottrell, C., et al. 2022, *MNRAS*, 516, 4354, doi: [10.1093/mnras/stac1962](https://doi.org/10.1093/mnras/stac1962)
- Yang, Y., Zabludoff, A. I., Zaritsky, D., & Mihos, J. C. 2008, *ApJ*, 688, 945, doi: [10.1086/591656](https://doi.org/10.1086/591656)
- Yu, N., Ho, L. C., & Wang, J. 2022a, *ApJ*, 930, 85, doi: [10.3847/1538-4357/ac5f07](https://doi.org/10.3847/1538-4357/ac5f07)
- Yu, N., Ho, L. C., Wang, J., & Li, H. 2022b, *ApJS*, 261, 21, doi: [10.3847/1538-4365/ac626b](https://doi.org/10.3847/1538-4365/ac626b)
- Zhang, C.-P., Zhu, M., Jiang, P., et al. 2024, *Sci. China Phys. Mech. Astron.*, 67, 219511, doi: [10.1007/s11433-023-2219-7](https://doi.org/10.1007/s11433-023-2219-7)
- Zwaan, M. A., Kuntschner, H., Pracy, M. B., & Couch, W. J. 2013, *MNRAS*, 432, 492, doi: [10.1093/mnras/stt496](https://doi.org/10.1093/mnras/stt496)